Rock fluidisation during peak-ring formation of large impact structures

Ulrich Riller[1]*, Michael H. Poelchau[2], Auriol S.P. Rae[3], Felix M. Schulte[1], Gareth S. Collins[3], H. Jay Melosh[4], Richard A.F. Grieve[5], Joanna V. Morgan[3], Sean P.S. Gulick[6], Johanna Lofi[7], Abdoulaye Diaw[7], Naoma McCall[6], David A. Kring[8], and IODP-ICDP Expedition 364 Science Party

[1] Institut für Geologie, Universität Hamburg, Bundesstrasse 55, 20146 Hamburg, Germany
[2] Universität Freiburg, Geologie, Albertstr. 23b, 79104 Freiburg, Germany
[3] Department of Earth Science and Engineering, Imperial College London, UK
[4] Department of Earth, Atmospheric, and Planetary Sciences, Purdue University, West Lafayette, IN 47907, USA
[5] Centre for Planetary Science and Exploration, Western University, London, Ontario, N6A 3K7, Canada
[6] Institute for Geophysics, University of Texas, Austin, TX, USA
[7] Géosciences Montpellier, Université de Montpellier, France
[8] USRA-Lunar and Planetary Institute, 3600 Bay Area Blvd., Houston TX 77058, USA
* Author for correspondence: ulrich.riller@uni-hamburg.de

Large meteorite impact structures on the terrestrial bodies of the solar system contain pronounced topographic rings, which emerged from uplifted target rocks within minutes of impact. In order to flow rapidly over large distances, these target rocks need to weaken drastically, but subsequently have to regain sufficient strength to build and sustain topographic rings. The mechanisms of rock deformation that accomplish such extreme change in mechanical behaviour during cratering are largely unknown and have been debated for decades. Recent IODP-ICDP drilling of the ~200-km diameter Chicxulub impact structure, Mexico, unveiled an unprecedented record of brittle and viscous deformation within its peak-ring rocks. Here, we show how catastrophic rock weakening upon impact is followed by an increase in rock strength that culminated in peak-ring formation during cratering. The observations point to quasi-continuous rock flow and, thus, acoustic fluidisation as the dominant physical process controlling initial cratering followed by increasingly localised faulting.

Large hypervelocity impact structures show a distinct size-morphology progression[1] (Fig. 1), which depends on the gravity and target rock type of the impacted body. In this regard, the study of internal topographic rings, the so-called peak rings[2], are of particular importance in understanding the formation of peak-ring impact structures (Fig. 1b) and multi-ring impact basins (Fig. 1c)[3]. As crater diameter increases beyond the maximum size of a bowl-shaped crater, the depth-diameter ratio of the crater decreases. On Earth, peak-ring crater formation (Fig. 2, Supplementary Information), takes place in minutes[1,4] and implies extreme deformation rates accompanying large displacements. Peak-ring craters can be a few hundred kilometres in diameter, yet merely a few kilometres deep, with the peak rings significantly elevated above crater floors. To explain this topographic characteristic, peak-ring crater formation requires drastic mechanical weakening of the target rocks. Weakening is thought to be caused by a decrease in the angle of internal friction and cohesion and results in large-scale fluid-like behaviour of target rock during part of the cratering process[4,5,6,7]. Towards the end of the cratering process, however, rock strength needs to be sufficiently high in order to form and sustain topographically elevated peak rings.

A number of mechanisms for target-rock weakening have been proposed. These include impact-induced fracturing and fragmentation of the target rocks[8-16], wholesale thermal softening by shock heating[6], fault weakening[17] by shear heating[18] or other processes, and acoustic fluidisation[19,20]. In this last process, short-wavelength, high-frequency pressure oscillations around the lithostatic pressure temporarily reduce the overburden pressure and, thus, friction between fractured target rocks.

Due to extremely limited ground-truth observations, the exact mechanisms and duration of target rock weakening during large impact cratering are unknown. In particular, unequivocal physical evidence for acoustic fluidisation or fault weakening in large impact craters remains to be identified. Large extra-terrestrial craters can only be analysed by remote sensing, which provides little or no subsurface structural information. With estimated original diameters between 180 and 250 km, Vredefort (South Africa), Sudbury (Canada) and Chicxulub (Mexico), known as "the big three" [21], are the largest impact structures known on Earth. Vredefort and Sudbury, however, are eroded to variable depths of ~10 and ~5 km[22], respectively, and so are largely missing the upper and most displaced target rocks (Fig. 2d). Chicxulub is the sole near-pristine, large impact structure with a topographic peak ring on Earth (Fig. 1d)[23-27], but hundreds of metre thick post-impact sedimentary strata buried the impact structure hindering direct access to the target rocks. Recent drilling, however, into the target rocks that constitute the peak ring at Chicxulub through IODP-ICDP Expedition 364[24,28] provides unprecedented insight into target rock deformation, respective weakening mechanisms and peak-ring formation, in large-scale impact cratering.

Structural characteristics of target rock

A total of 829 m of core was recovered from Expedition 364 borehole M0077A, starting at 506 m below sea floor (mbsf) (Fig. 1d)[24,28]. The recovered core includes 112 m of post-impact pelagic carbonate rock, followed by 130 m of impact melt rock and suevite, and 587 m of pervasively shocked target rock. The target rock consists of coarse-grained, alkali-feldspar-rich granitoid rock hosting uniformly oriented, pre-impact mafic and felsic sheet intrusions (Extended Data Figure 1). At depths between 1220 and 1316 mbsf, the target rock is mingled with impact melt rock on the decimetre to metre scale. Elsewhere in the target rock, impact melt rock is rather sparse. Mean density (2.41 g cm^{-3}) and mean P-wave velocity (4.1 km s^{-1}) of the target rock are considerably lower than those of typical felsic basement rocks (>2.6 g cm^{-3} and >5.5 km s^{-1})[24,28]. These petrophysical characteristics indicate substantial mechanical modification of the rock, notably in terms of increased porosity[29].

The post-impact carbonate rock is unstrained. Pre-impact deformation, however, of the granitoid target rock is evident through the sporadic presence of weak shape-preferred orientations of alkali-feldspar, plagioclase, quartz and biotite. The grain-shape alignment of these minerals formed under high-grade metamorphic conditions, as indicated by viscous deformation of feldspars and quartz[28]. Crystal-plastic strain cannot account for the reduced density and P-wave velocity of the target rock. Consequently, impact processes, including the damage caused by the passage of the shock wave, and deformation during peak-ring formation, must have caused the anomalous geophysical properties of the target rock [29].

Observed shock-induced structures in the target rock consist of shatter cones, microscopic planar deformation features and planar fractures in quartz and feldspars, as well as kinked biotite[28]. Severe structural target rock modification is evident by brittle and viscous deformation structures, including: (1) pervasive, irregular grain-scale fractures, (2) zones of cataclasite and ultra-cataclasite, (3) striated shear faults, (4) crenulated mineral foliations, and (5) brittle-ductile band structures (Figs. 3, 4). The formation of (1) to (3) increases substantially the volume of deformed rock and, thus, accounts for the observed reduction in density and P-wave velocity[29].

The spatial distribution of macroscopic deformation structures indicates highly heterogeneous deformation in the target rock (Fig. 3). Microscopic inspection of the granitoid target rock reveals the pervasive presence of intra- and inter-granular dilation fractures displaying jigsaw fragment geometry (Fig. 4a). Zones of strongly comminuted material separate displaced mineral fragments (Fig. 4b). These cataclasite zones range in thickness from millimetres to centimetres (Fig. 4a-c, g) and

indicate local differential shearing during cataclastic deformation. Locally, cataclasite zones grade into, or are truncated by, flow-foliated ultra-cataclasite, characterized by alternating quartz- and feldspar-rich layers (Fig. 4d). Crystal-plastic distortion of plagioclase (Fig. 4e) and quartz (Fig. 4f) indicate that target rock accumulated some plastic strain prior to pervasive fracturing and cataclastic flow. Zones of (ultra)-cataclasite and crude mineral foliations, defined by the shape-preferred orientation of biotite and coarse layers of quartz and feldspars, are sporadically kinked (Fig. 4g, h). In summary, cataclastic deformation displays variable intensity throughout the cored target rock, which is evident by its localisation and variable degree of comminution.

A total of 602 shear faults, with well-defined slip lineations, were recorded in the granitoid target rock (Fig. 3), with the total number of shear faults being vastly higher. By contrast, only 13 shear faults with slip lineations were identified in the post-impact carbonate rock and consist of a few millimetre long calcite fibres (Fig. 4i), typical for seismic stick-slip faulting[30]. Slip lineations in the target rock, however, form pronounced ridges and grooves of strongly comminuted host rock material (Fig. 4k). Displacements on these faults may amount to several decimetres[28]. While the post-impact carbonate rock shows a weak tectonic overprint, it is evident that the granitoid target rocks underwent catastrophic and pervasive shear faulting.

At 1220 to 1316 mbsf, the target rock is strongly distorted and brecciated, and fragments of it are marginally resorbed and found in melt rock (Fig. 5a, b). Conversely, zones of brecciated target rock host elongate, and frequently wispy, melt-rock fragments, reminiscent of suevite (Fig. 5c, d). Where in contact with target rock fragments, the melt rock underwent large ductile strains, as evident by highly stretched granitoid fragments contained in the melt rock (Fig. 5e). Overall, the melt rock is spatially associated with the highest-strained target rocks, indicated by up to decimetre- to metre-thick breccia. The presence of exotic fragments (Fig. 5f), consisting of gneiss, mafic igneous rock and various mylonites, in the melt rock excludes an *in-situ* frictional melt origin for the melt rock. Breccia zones are substantially thicker and show a larger range in sizes and shapes of fragments than cataclasite and ultra-cataclasite zones in target rock outside this particular depth interval. The differences in thickness and fragment size between these breccia and the cataclasite zones indicate different fragmentation mechanisms and/or fragmentation at different times during the cratering process. Finally, the spatial density of ductile band structures is maximal within this depth interval (Fig. 3). Brittle-ductile band structures occur predominantly in mechanically and thermally weakened target and melt rock and form ductile shear zones (Fig. 5f), shear bands with C-S fabric geometry (Fig. 5g)[31] and crenulated mineral fabrics (Fig. 4h).

Chronology of deformation mechanisms

Most importantly, it is possible to determine the relative timing of the various deformation mechanisms. Zones of (ultra-)cataclasite truncate the jigsaw fragment geometry of pervasively fractured target rock (Fig. 4a, b). Shear faults, in turn, consistently offset cataclasite and ultra-cataclasite zones (Fig. 4c). Target rock fragments in melt rock are sporadically striated and host cataclasite zones[28]; whereas melt rock matrices are devoid of shear faults. Cataclasite and melt rock are found in tension fractures (Fig. 5h), which, to some extent, formed from shear faults. Brittle-ductile band structures displace zones of cataclasite, crenulated foliation surfaces and the contacts of target rock with cataclasite and melt rock (Figs. 4g, h, 5f, g). In summary, pervasive fracturing of target rock was followed, respectively, by formation of (ultra-)cataclasite zones, shear faulting, emplacement of cataclasite and impact melt into dilatant fractures, and formation of ductile band structures.

Deformation mechanisms and cratering stages

During the various cratering stages, deformation kinematics and states of stress of the target rock differ profoundly (Fig. 2). Therefore, distinct deformation mechanisms recognized in the target rock may well relate to individual cratering stages denoted in terms of time (T) after impact. Shock and decompression causes irreversible plastic deformation and imparts to the shocked rocks a divergent outward velocity field which forms the transient cavity. This velocity field causes wall-parallel extension and perpendicular shortening of the target rock (Fig. 2b). Rock deformation at upper-crustal pressures and depths, from where peak-ring materials are derived, is accommodated by fracturing. We, therefore, attribute pervasive fracturing, which preceded the other deformation mechanisms, to shock loading, decompression, and transient cavity growth ($T < 30$ s).

After the transient cavity forms (Fig. 2b), gravitational collapse modifies the crater shape until the final crater morphology is reached (Supplementary Information). During initial collapse, the peak-ring material motion transitions from outward and divergent excavation flow to inward and convergent rock flow toward the crater centre. This inward movement leads to the incorporation of peak-ring material onto the flank of a central uplift (Fig. 2c). During this stage of cratering, peak-ring materials experience several distinct stress states (Extended Data Figure 2). Planar zones of cataclasite and (ultra-)cataclasite are plausible candidates for accommodating the deformation of pre-fractured target rock during this cratering stage ($20 \text{ s} < T < 150$ s).

During build-up of the central uplift ($20 \text{ s} < T < 100$ s), the pressure on the peak-ring material increases (Extended Data Figure 2). This increase inevitably closes asperities within the fractured rock and, thus, increases the internal friction of the target rock and normal stresses on faults. The central uplift eventually over-heightens and becomes gravitationally unstable, causing downwards and radial-outward collapse ($160 \text{ s} < T < 300$ s). In this motion, collapsed material piles up to form the peak ring, which is thrust over the inwardly slumped transient cavity rim (Fig. 2d, Supplementary Information). Collectively, the increased pressure, combined with the reversal of the material displacement field as the central uplift transitions from motion upwards to outwards and downwards during collapse accounts for the observed transition from localised cataclastic flow to shear faulting during this stage of cratering.

As the melt rock occurrences within the target rock are devoid of shear faults, melt emplacement must occur at the end of peak-ring formation ($250 \text{ s} < T < 600$ s). Subsequent deformation is evident by ductile band structures displacing contacts between the target and melt rock, zones of cataclasite and mineral foliations. Band orientation, sense of displaced layers and fabric asymmetry, displayed by sigmoidal foliation planes and cataclasite zone boundaries, consistently indicate band formation through normal faults (Figs. 4g, h, 5f, g). Respective vertical shortening and horizontal extension is consistent with gravitational spreading of the topographically elevated peak ring and signifies the final stage of crater modification (inset in Fig. 2d).

Weakening mechanisms

The recognition of distinct deformation mechanisms corresponding to the various stages of the cratering process is of fundamental importance in comprehending the mechanics of large-scale impact cratering. Initial pervasive grain-scale fracturing causes a profound loss of cohesion in target rocks at the onset of, and during, transient cavity growth. During cavity modification, strain is localised progressively through formation of cataclasite zones, ultra-cataclasite zones, shear faults, and finally deformation on fault zones with impact-melt bearing fault breccias. Progressive strain localisation is evidence of the incremental regaining of shear and cohesive strength in the target rock, as crater modification proceeds. It has been proposed that crater collapse is facilitated by the self-lubrication of faults by frictional melts[18]. We did not, however, uncover any evidence for friction-

generated melt rock in the recovered target rock from the peak ring at Chicxulub. Hence, dynamic weakening of faults, if significant, appears to require a mechanism other than shear heating.

Shock compression and dilation during initial impact caused wholesale intra-crystalline damage (Fig. 4e, f). Thereafter, dynamic fracturing induced by the passage of the shock and rarefaction waves and transient cavity growth led to loss in cohesion and shear strength. The presence of pervasively fractured target rock with preserved microscopic jigsaw fragment patterns and uniform orientation of pre-impact dikes (Extended Data Figure 1) indicate that target rock above 1220 mbsf behaved largely as a structurally coherent rock mass. The implication of small displacements across the entire rock mass is consistent with macroscopic deformation of an acoustically fluidised rock mass[19,20].

Structural observations from the peak-ring target rocks of Chicxulub are generally consistent with acoustic fluidisation as the dominant weakening mechanism and offer insight for the refinement of future impact simulations. Acoustic fluidisation entails target rock blocks undergoing pressure oscillations around the ambient lithostatic stress[4,7,19,20]. During pressure lows, blocks have reduced normal stresses between them, drastically reducing frictional resistance at block boundaries during periodic rock flow. During pressure highs, blocks are compressed, locally increasing the frictional resistance of the deforming rock mass. Cataclasite zones are prime candidates for the physical expression of the sheared block boundaries serving as contact strain zones, during oscillation of target rock blocks. Continued cataclasis, resulting in flow-foliated ultra-cataclasite, heralds an increase in shear strain of the rock mass and waning acoustic fluidisation. While in motion, continued comminution in (ultra)-cataclasite zones may generate additional acoustic energy and prolong cataclastic flow[15].

A critical parameter in the acoustic fluidisation model is the dominant wavelength of pressure vibrations[19], which controls both the viscosity of the acoustically fluidized rock mass and the timescale for the decay of vibrations. The “block model” of acoustic fluidisation is employed in most Chicxulub-scale impact simulations[4,23,24], such as the one reproduced in Fig. 2. The block model supposes that the subcrater rock mass is dominated by blocks of a characteristic size that oscillate within a surrounding mass of breccia with a single vibrational wavelength (and period) that is directly proportional to the block size[32]. The block model parameters employed in Chicxulub impact simulations imply a block size of about 100-500 m (depending on the assumed acoustic energy dissipation factor Q) and an oscillation frequency of a few Hz. This prediction is consistent with the entire ~450-m granite sequence above the imbricate thrust zone representing a single “block”.

On the other hand, if the cataclasite zones observed in the Chicxulub peak-ring drill core represent oscillating-block boundaries as we propose, their average spacing (Fig. 3) of about 3.5 m (2.3 m including ultra-cataclasite zones) would imply a much smaller block size, shorter dominant vibrational wavelength and higher vibrational frequency[19,20]. The implied rapid evolution of the acoustic wave field during collapse of the crater is not predicted by the current block model implementation. Sustaining high-frequency vibrations, however, for the duration of crater collapse could be explained by efficient regeneration of acoustic energy during the cratering process, which is neglected in the block model. Effective regeneration of vibrations in a rapidly shearing rock mass is consistent with findings from discrete-element models of acoustic fluidisation in landslides[33]. Alternatively, the acoustic wave field may evolve by progressive lengthening of the dominant vibrational wavelength during cratering as higher frequency vibrations dissipate sooner. In this case, the effective block size could increase during crater formation from a few metres at the beginning of modification, when the first cataclasite zones are likely to have formed (20 s < T < 60 s), to a few hundred metres by the end of peak-ring emplacement (T < 600 s).

A progressive waning of the acoustic wavefield in which slip events, facilitated by negative pressure excursions, become less frequent and more widely spaced is consistent with the temporal evolution of deformation observed in the drill core. This evolution suggests a progression from distributed, small-displacement deformation along closely spaced faults early in the cratering process to more localised, larger-displacement deformation along widely spaced slip-surfaces later. Acoustic fluidisation is, therefore, interpreted to halt at the onset of shear faulting, as target rock blocks cease to oscillate and the bulk rock mass regains internal friction and, thus, shear strength. Whether this cessation of acoustic fluidisation occurs during the final emplacement of the peak ring (as suggested by current numerical simulations; Fig. 2d) or earlier during the formation of the central uplift is unclear. In the latter scenario, the outward collapse of the central uplift and thrusting of peak-ring rocks onto the transient cavity rim occurred after the rocks regained most of their large-scale static strength. In this case, the late stages of collapse could have been facilitated by large faults, lubricated by entrained impact melt.

Peak-ring formation

Modelling suggests that the target rock forming the peak ring resided at a depth of ~10 km[24], prior to impact, and was entrained into a central uplift before being thrust outward over inward slumped transient cavity wall segments (Fig. 2). Based on the modelled cratering flow (Supplementary Information), it is conceivable that individual target rock blocks may over-thrust portions of impact melt, notably where the peak ring develops. Impact melt may then become sandwiched between quasi-coherent target rock masses. Hence, impact melt in large craters may be present not only as ponded liquids at surface, but also as melt bodies or sheets entrained and trapped in target rock thrust zones at depth.

Structural and lithological characteristics of the rocks at depths between 1220 and 1316 mbsf are consistent with impact melt entrained in a prominent thrust zone. Respective characteristics include: (1) the concentration of high strains in target rock and melt rock (Fig. 5a, e), (2) the strongly distorted target rock slivers mingled with melt rock and breccia, interpreted as fault breccia (Fig. 5a-d, f), (3) the occurrence of melt rock fragments in fault breccia (Fig. 5c, d, f), and (4) fragment lithologies not present in the adjacent target rock[28]. As *in situ* frictional melting is excluded for the origin of the melt rock, formation of this rock by shock-induced melting and subsequent entrainment during peak-ring formation appears the more plausible explanation. Specifically, we propose the target rock mass above 1220 mbsf over-thrust and buried the impact melt overlying the deeper target rock, now found below 1316 mbsf. Impact melt rock in contact with brecciated target rock displays large ductile strains (Fig. 5e) and indicates rapid cooling (quenching) and solidification of the impact melt during thrusting. In summary, imbricate thrusting (stacking) of target rock masses[34] contributed to the high topography of the peak ring. A prerequisite for thrusting is the regaining of shear strength in the target rock by the time of the formation of peak-ring topography.

Consequences of dynamic weakening

Examination of the deformation mechanisms of the target rocks underlying the peak ring at Chicxulub has provided unprecedented evidence for the physical mechanisms responsible for weakening and the regain in strength of target rock during large-scale impact cratering. Results are strongly supportive of the dynamic collapse model (Fig. 2, Supplementary Information) of peak-ring formation and of acoustic fluidisation as the dominant mechanism driving crater modification. The transition in deformation style from distributed cataclastic flow to localised shear-faulting and the progressive increase in fault spacing illuminates the waning of acoustic fluidisation and the target regaining sufficient strength to support the topography of the peak ring. Dynamic weakening of faults or regeneration of acoustic energy may play an important role in this final phase of peak-ring

formation. Incorporating this insight into future numerical impact simulations will aid in the design of higher-fidelity models of large-scale impact cratering.

Notably, (ultra)-cataclasite zones, serving as contact strain zones of oscillating target rock blocks, are regarded as the physical manifestation of pressure fluctuations. If so, the estimated average size of coherent target rock blocks within the Chicxulub peak ring is one to two orders of magnitudes smaller than observed in the central uplifts of smaller terrestrial complex craters[35,36,37]. This may imply efficient regeneration of pressure fluctuations during transient cavity collapse and modification or a growth in vibrational wavelength as the wavefield evolves. In either case, central peaks of smaller impact structures may be preserved because fluidisation ceased early in the gravitational collapse process. By contrast, peak rings in peak-ring craters and multi-ring basins form because acoustic fluidisation is sustained through the formation and collapse of an overheightened central uplift.

References

1. Croft, S.K. The modification stage of basin formation: Conditions of ring formation. In Multi-Ring Basins, Proceedings of the 12th Lunar and Planetary Science Conference: *Geochimica et Cosmochimica Acta* **12A** (P. H. Schultz and R. B. Merrill, Eds.), 227-257. Pergamon, Elmsford, NY (1981).

2. Grieve, R. A. F., Robertson, P.B. & Dence, M. R. Constraints on the formation of ring impact structures, based on terrestrial data. In Multi-Ring Basins, Proceedings of the 12th Lunar and Planetary Science Conference: *Geochimica et Cosmochimica Acta* **12A** (P. H. Schultz and R. B. Merrill, Eds.), 37–57. Pergamon, Elmsford, NY (1981).

3. Neumann, G. A., Zuber, M. T., Wieczorek, M. A., Head, J. W., Baker, D. M. H., Solomon, S. C., Smith, D. E., Lemoine, F. G., Mazarico, E., Sabaka, T. J., Goossens, S. J., Melosh, H. J., Phillips, R. J., Asmar, S. W., Konopliv, A. S., Williams, J. G., Sori, M. M., Soderblom, J. M., Miljković, K., Andrews-Hanna, J. C., Nimmo, F. & Kiefer, W. S. Lunar impact basins revealed by gravity recovery and interior laboratory measurements. *Science Advances* **1**, e1500852 (2015).

4. Ivanov, B. A. Numerical modelling of the largest terrestrial meteorite craters. *Sol. Sys. Res.* **39,** 381-409 (2005).

5. Melosh, H. J & Ivanov, B. A. Impact crater collapse. *Ann. Rev. Earth Planet. Sci.* **27,** 385-415 (1999).

6. O' Keefe, J. D., & Ahrens, T. J. Planetary cratering mechanics. *J. Geophys. Res.* **98**, 17,011–17,028 (1993).

7. Wünnemann, K. & Ivanov, B. A. Numerical modelling of the impact crater depth-diameter dependence in an acoustically fluidized target. *Planet. Space Sci.* **51,** 831-845 (2003).

8. Grady, D. E. & Kipp, M. E. Dynamic rock fragmentation. In: Fracture Mechanics of Rock, Academic Press, London, UK, 429–475 (1987).

9. Fujiwara, A., Kamimoto, G. & Tsukamoto, A. Destruction of basaltic bodies by high-velocity impact. *Icarus* **31**, 277-288 (1977).

10. Ahrens, T. J. & Rubin, A. M. Impact-induced tensional failure in rock. *J. Geophys. Res.* **98**, 1185-1203 (1993).

11. Buhl. E., Kowitz A., Elbeshausen D., Sommer F., Dresen G., Poelchau M. H., Reimold W. U., Schmitt, R. T. & Kenkmann, T. Particle size distribution and strain rate attenuation in hypervelocity impact and shock recovery experiments. *J. Struc. Geol.* **56**, 20-33 (2013).

12. Collins, G. S. Numerical simulations of impact crater formation with dilatancy. *J. Geophys. Res.* **119**, 2600-2619 (2014).

13. Melosh, H. J., Ryan, E. V. & Asphaug, E. Dynamic fragmentation in impacts: hydrocode simulation of laboratory impacts. *J. Geophys. Res.* **97**, 14,735-14,759 (1992).

14. Kenkmann, T. Folding within seconds. *Geology* **30,** 231-234 (2002).

15. Kenkmann, T. Dike formation, cataclastic flow, and rock fluidization during impact cratering: an example from the Upheaval Dome structure, Utah. *Earth Planet. Sci. Lett.* **214**, 43-58 (2003).

16. Collins, G. S., Melosh, H. J. & Ivanov, B. A. Modeling damage and deformation in impact simulations. *Meteorit. & Planet. Sci.* **39**, 217-231 (2004).

17. Senft, L. E. & Stewart, S. T. Dynamic fault weakening and the formation of large impact craters. *Earth Planet. Sci. Lett.* **287**, 471-481 (2009).

18. Spray, J. G. Superfaults. *Geology* **25**, 579-582 (1997).

19. Melosh, H. J. Acoustic fluidization: a new geological process? *J. Geophys. Res.* **84,** 7513-7520 (1979).

20. Melosh, H. J. Dynamical weakening of faults by acoustic fluidization. Nature **379**, 601-606 (1996).

21. Grieve, R. A. F. & Therriault, A. Vredefort, Sudbury, Chicxulub: Three of a kind? *Annu. Rev. Earth Planet. Sci.* **28**, 305–338 (2000).

22. Grieve, R. A. F., Reimold, W. U., Morgan, J., Riller, U. & Pilkington, M. Observations and Interpretations at Vredefort, Sudbury and Chicxulub: Towards a composite kinematic model of terrestrial impact basin formation. *Met. & Planet. Sci.* **43**, 855-882 (2008).

23. Collins, G. S., Melosh, H. J., Morgan, J. V. & Warner, M. R. Hydrocode simulations of Chicxulub crater collapse and peak-ring formation. *Icarus* **157,** 24-33 (2002).

24. Morgan, J. V., Gulick, S. P. S., Bralower, T., Chenot, E., Christeson, G., Claeys, P., Cockell, C., Collins, G. S., Coolen, M. J. L., Ferrière, L., Gebhardt, C., Goto, K., Jones, H., Kring, D. A., Le Ber, E., Lofi, J., Long, X., Lowery, C., Mellett, C., Ocampo-Torres, R., Osinski, G. R., Perez-Cruz, L., Pickersgill, A., Poelchau, M., Rae, A., Rasmussen, C., Rebolledo-Vieyra, M., Riller, U., Sato, H., Schmitt, D.R., Smit, J., Tikoo, S., Tomioka, N., Urrutia-Fucugauchi, J., Whalen, M., Wittmann, A., Yamaguchi, K. E. & Zylberman, W. The formation of peak rings in large impact craters. *Science* **354**, 878-882 (2016).

25. Morgan, J. V., Warner, M. R., Collins, G. S., Melosh, H. J. & Christeson, G. L. Peak-ring formation in large impact craters: Geophysical constraints from Chicxulub. *Earth Planet. Sci. Lett.* **183**, 347-354 (2000).

26. Morgan, J. V., Warner, M. R., Collins, G. S., Grieve, R. A. F., Christeson, G. L., Gulick, S. P. S. & Barton, P. J. Full waveform tomographic images of the peak ring at the Chicxulub impact crater. *J. Geophys. Res.* **116**, B06303 (2011).

27. Gulick, S. P. S, Barton, P. J., Christeson, G. L., Morgan, J. V., McDonald, M., Mendoza-Cervantes, K., Pearson, Z. F., Surendra, A., Urrutia-Fucugauchi, J., Vermeesch, P. M. & Warner, M. R. 2008.

Importance of pre-impact crustal structure for the asymmetry of the Chicxulub impact crater. *Nature Geoscience* **1**, 131-135.

28. Morgan, J. V., Gulick, S. P. S., Mellet, C. L., Green, S. L. & Expedition 364 Scientists. Chicxulub: Drilling the K-Pg Impact Crater, Proceedings of the International Ocean Discovery Program, 364, International Ocean Discovery Program, College Station, Texas (2017).

29. Christeson, G. L., Gulick, S. P. S., Morgan, J. V., Gebhardt, C., Kring, D. A., LeBer, E., Lofi, J., Nixon, C., Poelchau, M., Rae, A. S. P., Rebolledo-Vieyra, M., Riller, U., Schmitt, D. R., Wittmann, A., Bralower, T. J., Chenot, E., Claeys, P., Cockell, C. S., Coolen, M. J. L., Ferrière, L., Green, S., Goto, K., Jones, H., Lowery, C. M., Mellett, C., Ocampo-Torres, R., Perez-Cruz, L., Pickersgill, A. E., Rasmussen, C, Sato, H., Smit, J., Tikoo, S. M., Tomioka, N., Urrutia-Fucugauchi, J., Whalen, M. T., Xiao, L., & Yamaguchi, K. E. Extraordinary rocks from the peak ring of the Chicxulub impact crater: P-wave velocity, density, and porosity measurements from IODP/ICDP Expedition 364. Earth Plant. Sci. Let. **495**, 1-11 (2018).

30. Petit, J. P. Criteria for the sense of movement on fault surfaces in brittle rocks. *J. Struct. Geol.* **9**, 597–608 (1987).

31. Berthé, D., Choukroune, P. & Jegouzo, P. Orthogneiss, mylonite and non-coaxial deformation of granites: the example of the South Armorican Shear Zone. *J. Struct. Geol.* **1**, 31-42 (1979).

32. Ivanov, B. A. & Artemieva, N. A. Numerical Modeling of the Formation of Large Impact Craters. In Catastrophic Events and Mass Extinctions: Impact and Beyond. *Geol. Soc. of America Special Paper* **356** (C. Koeberl and K. G. MacLeod, Eds.), 619–630 (2002).

33. Johnson, B. C., Campbell, C. S. & Melosh, H. J. The reduction of friction in long runout landslides as an emergent phenomenon. *J. Geophys. Res.* **121**, 881-889 (2016).

34. Kring, D. A., Kramer, G. Y., Collins, G. S., Potter, R. W. K. & Chandnani, M. Peak-ring structure and kinematics from a multi-disciplinary study of the Schrödinger impact basin. *Nature Communications* **7**, 13167 (2016).

35. Ivanov, B. A., Kocharyan, G. G. & Kostuchenko, V. N. Puchezh-Katunki impact crater: preliminary data on recovered core block structure (abstract). 27th Lunar and Planetary Science Conference, 589–590 (1996).

36. Kenkmann, T., Collins, G. S. & Wünnemann, K. The modification stage of crater formation. In: Osinski, G. R., Pierazzo, E. (Eds.), Impact Cratering: Processes and Products. John Wiley & Sons, Chichester, 60-75 (2013).

37. Rae, A. S. P, Collins, G. S., Grieve, R. A. F., Osinski, G. R. & Morgan, J. V. Complex crater formation: Insights from combining observations of shock pressure distribution with numerical models at the West Clearwater Lake impact structure. Met. & Planet. Sci. **52**, 1330-1350 (2017).

Acknowledgments

This work was supported by the Priority Program 527 of the German Science Foundation (grants Ri 916/16-1 and PO 1815/2-1), National Science Foundation grants (OCE-1737351, OCE-1450528, OCE-1736826), and Natural Environment Research Council (grants NE/P011195/1 and NE/P005217/1). The Chicxulub drilling expedition was funded by the European Consortium for Ocean Research Drilling (ECORD) and the International Ocean Discovery Program (IODP) as Expedition 364 with co-funding from the International Continental Scientific Drilling Program (ICDP). The Yucatan State

Government and Universidad Nacional Autónoma de México (UNAM) provided logistical support. This research used samples and data provided by IODP. Samples can be requested at http://web.iodp.tamu.edu/sdrm. We are grateful for assistance of the staff of the IODP Core Repository in Bremen, Germany for their assistance during the Onshore Science Party. Boris Ivanov and Christian Koeberl are thanked for insightful and constructive reviews. We thank Stephanie Teuber for assistance in figure preparation. This is UTIG Contribution #3278.

Author contribution statement

U.R., M.H.P., A.S.P.R., J.V.M., S.P.S.G., and R.A.F.G conceived the study. All authors participated in sampling and data collection offshore and/or onshore during IODP-ICDP Expedition 364, interpretation of the data as well as writing and/or editing of the manuscript. U.R. provided the first draft of the manuscript. U.R. and F.M.S. acquired structural data from line scans. J.L. and A.D. provided the downhole orientation data. A.S.P.R and G.S.C. performed and analysed the numerical models; G.S.C., A.S.P.R. and H.J.M. contributed the discussion on the implications for acoustic fluidisation.

Competing interests The authors declare no competing interests.

Correspondence and requests for materials should be addressed to U.R.

Main figure legends

Figure 1: Typical impact structures of the Moon (http://quickmap.lroc.asu.edu) and geophysical characteristics of the Chicxulub impact structure. Topographically elevated areas in (a) to (c) are highlighted in magenta. (a) Central-peak crater: Tycho (diameter: 85 km), (b) Peak-ring impact structure: Schrödinger[34] (diameter: 312 km), (c) Multi-ring impact basin: Orientale (diameter: 930 km). (d) Combined gravity and seismic line A[27] of the Chicxulub impact structure. Offshore seismic data[27] indicate that the Chicxulub peak ring roughly correlates with a gravity low. The location of drill hole M0077A on the peak ring is indicated.

Figure 2: Formation of the Chicxulub impact structure based on numerical modelling of peak-ring crater formation[4,23,24,34]. A grid of tracer particles is shown to highlight the sub-crater deformation. Dark red area of crust in each panel tracks the material that eventually forms the peak ring. T denotes time in seconds after impact. Red half arrows indicate the direction of major shear displacements relative to adjacent material. (a) Undisturbed configuration of model lithosphere prior to impact. (b) Cratering starts by shock wave-induced, crustal-scale excavation of a bowl-shaped transient cavity. (c) Gravitational instability of the transient cavity causes uplift of the crater centre and concomitant inward slumping of the cavity wall. (d) Collapse and radial outward displacement of uplifted material over inward-slumped cavity wall segments followed by gravitational settling of the peak ring (inset) characterize the terminal phase of modelled crater modification. White lines indicate approximate current erosion levels of the Sudbury and Vredefort impact structures.

Figure 3: Spatial distribution of major lithological units and deformation structures in target rock of M0077A drill core. Note the strong spatial correlation of increased numbers of (ultra-)cataclasite zones, crenulated foliations and ductile band structures below 1220 mbsf.

Figure 4: Deformation structures in target rock at Site M0077A. Arrow indicates top direction of drill core. (a) Photomicrograph in plane-polarized light showing pervasive cataclasite of granitoid target rock (core 122-3, 820 mbsf). (b) Line drawing of (a) showing alkali-feldspar (Kf) displaced on cataclasite zone (c). (c) Cataclasite zones displaced on shear faults (core 301-1, 1326.45-1326.57 mbsf). (d) Flow-foliated ultra-cataclasite (core 215-2, 1065.85-1065.94 mbsf). (e) Photomicrograph in cross-polarized light showing distorted twin lamellae in plagioclase (core 129-1, 831.38-831.40 mbsf). (f) Photomicrograph in cross-polarized light showing distorted quartz with planar deformation features (core 129-1, 831.38-831.40 mbsf). (g) Cataclasite zone segmented by normal faults (core 172-2, 956.41-956.45 mbsf). (h) Crenulated layering in granitoid rock (core 122-1, 817.61-817.66 mbsf). (i) Striated shear fault in carbonate rock. (k) Striated shear fault in granitoid target rock (core 154-1, 894.19 mbsf).

Figure 5: Images illustrating highly distorted granitoid rock (g), impact melt rock (m), fault breccia (b) and exotic fragments (e) between 1220 and 1316 mbsf. (a) Line scan of core 265-2 (1216.36-1217.45 mbsf) showing highly distorted and brecciated target rock mingled within melt rock. Note halos of mingled melt rock and fault breccia at the margins of granitoid rocks as well as shear faults displacing thin zones of ultra-cataclasite. (b) Line drawing of (a). (c) Line scan of core 285-1 (1277.24-1278.25 mbsf) displaying mingling of impact melt rock and fault breccia notably near granitoid fragment. Note melt rock fragments within fault breccia. (d) Line drawing of (c). (e) Melt rock in contact with fault breccia. Note gradient in contact strain evident by stretched target rock fragments in melt rock (core 303-3, 1334.24-1334.35 mbsf). (f) Ductile shear zone in mingled impact melt rock and fault breccia containing exotic fragments (core 289-1, 1289.75-1289.87 mbsf). (g) C-S fabric geometry in granitoid indicated by displaced planar mineral fabric in granitoid target rock (half arrows) amounting to vertical shortening and horizontal extension (white arrows) (core 273-2, 1241.26-1241.31 mbsf). (h) Cataclasite entrained in dilatant fracture (core 262-1, 1207.45-1207.56 mbsf).

Methods

Acquisition of structural data from drill core

In addition to the methods employed for visual appraisal as well as meso- and microstructural analyses of the drill core during the Onshore Science Party[38], the following analyses were conducted. Based on a detailed examination of drill core line-scans, the occurrence of cataclasite zones, ultra-cataclasite zones, crenulated foliations and ductile band structures was recorded with depth. Only zones of (ultra-)cataclasite displaying a thickness of 1 centimeter and larger were recorded. Distinction between the two types of cataclasite is based on grain size, the presence of flow foliation and the fragment-size distribution. Overall, ultra-cataclasite appears darker than cataclasite. Mesoscopic shear faults displaying slip lineations and slip sense were identified by carefully removing core sections from the liners. Statistical analysis of the spatial occurrence of the structures were conducted with Microsoft Excel (Source Date Figure 3).

Microstructural analysis

Polished thin sections of 25 µm thickness were produced from selected target rock samples at the Institute of Mineralogy and Petrography of the University of Hamburg, Germany. Microscopic inspection of thin sections was conducted using a Zeiss Axio Scope.A1 polarization microscope and attached high-resolution digital camera AxioCam MRc Rev. 3 FireWire.

Borehole imaging of planar structures

During Expedition 364, both optical and acoustic borehole images of the borehole walls were acquired[38]. Post-acquisition processing and analysis allowed manual picking of the planar structural discontinuities corresponding to pre-impact igneous sheet intrusions, and determining their orientation. Orientations have not been corrected from borehole deviation, which departs less than 4° from the vertical. For visualization and processing of borehole images, the ALT WellCAD software package was used. For analysis of orientation of pre-impact sheet intrusions the software package Tectonics FP version 1.6 was used[39].

Numerical modelling

To aid interpretation of the drill core data, we reproduced and reprocessed the numerical simulation of the Chicxulub impact[24], which was in turn based on previous Chicxulub impact simulations that produced a good match to geological and geophysical constraints[4,23,32,40]. The impactor parameters of the model were: diameter = 14 km, velocity = 12 km/s, density = 2650 kg/m^3. A vertical incidence impact angle was enforced by the cylindrical geometry of the two-dimensional model. A spatial resolution of 200 m was used, corresponding to 35 cells across the impactor radius. A simplified target structure was used of 3-km (carbonate) cover rocks, 30-km (granite) crust overlying (dunite) mantle. The simulation duration was 600 seconds of model time. We refer to Morgan et al. (2016)[24] for a full description of the modelling approach, including a comprehensive list of model parameters.

Simulations were processed to examine the motion and pressure of peak-ring materials (Fig. 2a-d, Extended Data Figure 2 and animation in Supplementary Information). Lagrangian tracer particles employed in the numerical method allow the history of material that ends up within the peak ring to be recorded and interrogated. Morgan et al. (2016)[24] used tracer particles to illustrate the peak pressure and provenance of the peak-ring materials, as well as its motion during crater formation. Here, we identified a subset of 100 tracer particles within the same peak-ring material, initially located within a square (2 km x 2 km) cross-section at a depth of 10 km and a radius of 16 km (see Supplementary Information, T = 0). Animation in Supplementary Information shows the motion of these tracers during cratering in both the fixed simulation reference frame (main image) and in a Lagrangian reference frame, centred on the average location of the 100 tracers (inset). The inset image gives a qualitative sense of the internal deformation of the peak-ring materials and highlights the deformation kinematics of peak-ring material during cratering.

Additionally, we analysed the pressure recorded by each tracer (circles) within this same volume, as well as the average pressure (solid line), as a function of time during the simulation (Extended Data Figure 2). After the brief passage of the shock wave (P > 10 GPa; T < 5 s), the pressure in the peak-ring materials rises from 10-20 MPa to 50-100 MPa between ~100 and ~250 s, before returning back to 10-20 MPa. Thus, the inward collapse of the peak-ring materials toward the central uplift and the subsequent outward collapse are associated with elevated pressures, above the ultimate overburden pressure in the peak-ring materials at their final location. We note that pressure waves caused by shockwave reflections from the numerical domain boundaries, which would not be present in reality, are superimposed on the pressure-time signal after ~130 s. While these complicate interpretation, the elevated pressure for the two minutes of central uplift formation and collapse is a robust outcome of the model that is insensitive to the location of the domain boundary.

Data availability. All data generated or analysed during this study are included in this published article (and its supplementary information files). Other Expedition 364 data are available online (https://doi.org/10.14379/iodp.proc.364.2017).

References cites in online Methods section

38. Gulick, S., Morgan, J., Mellett, C.L., Green, S.L., Bralower, T., Chenot, E., Christeson, G., Claeys, P., Cockell, C., Coolen, M., Ferrière, L., Gebhardt, C., Goto, K., Jones, H., Kring, D., Lofi, J., Lowery, C., Ocampo-Torres, R., Perez-Cruz, L., Pickersgill, A.E., Poelchau, M., Rae, A., Rasmussen, C., Rebolledo-Vieyra, M., Riller, U., Sato, H., Smit, J., Tikoo, S., Tomioka, N., Urrutia-Fucugauchi, J., Whalen, M., Wittmann, A., Yamaguchi, K., Xiao, L., & Zylberman, W., and the Expedition 364 ESO Team. Expedition 364 Methods, in Proceedings of the International Ocean Discovery Program Volume 364 (Morgan, J., Gulick, S., Mellett, C.L., Green, S.L., and the Expedition 364 Scientists, Eds.), 1-46. (2017).

39. Ortner, H., Reiter, F., & Acs, P. Easy handling of tectonic data: the programs tectonics FP for mac and tectonics FP for windows. Comput. Geosci. **28**, 1193-1200 (2002).

40. Collins, G.S., Morgan, J.V., Barton, P., Christeson, G.L., Gulick, S., Urrutia-Fucugauchi, J., Warner, M.R., Wünnemann, K. Dynamic modeling suggests terrace zone asymmetry in the Chicxulub crater is caused by target heterogeneity. *Earth Planet. Sci. Lett.* **270**, 221–230 (2008).

Extended Data figure legends

Extended Data Figure 1: Lower-hemisphere, equal-area diagrams showing poles to pre-impact aplite, pegmatite and diabase sheet intrusions.

Extended Data Figure 2: Diagram showing pressure vs time as recorded by 100 Lagrangian tracer particles in the peak-ring rocks (see animation of Supplementary Information for location of tracer particles). Grey circles show the pressure of each tracer particle at time intervals of 2 seconds. Black solid line shows average pressure (all tracer particles). Note the elevated pressures between T = 100 s and T = 250 s during central uplift formation and collapse.

a

N

25 km

b

N

75 km

c

N

200 km

d

21°N

21°30'N

89°W

90°W

N

Chicxulub

Mérida

M0077A

5 km

10 km

15 km

Gravity (mgal)

-30 -16 -10 0 10 20 30 40 50 64

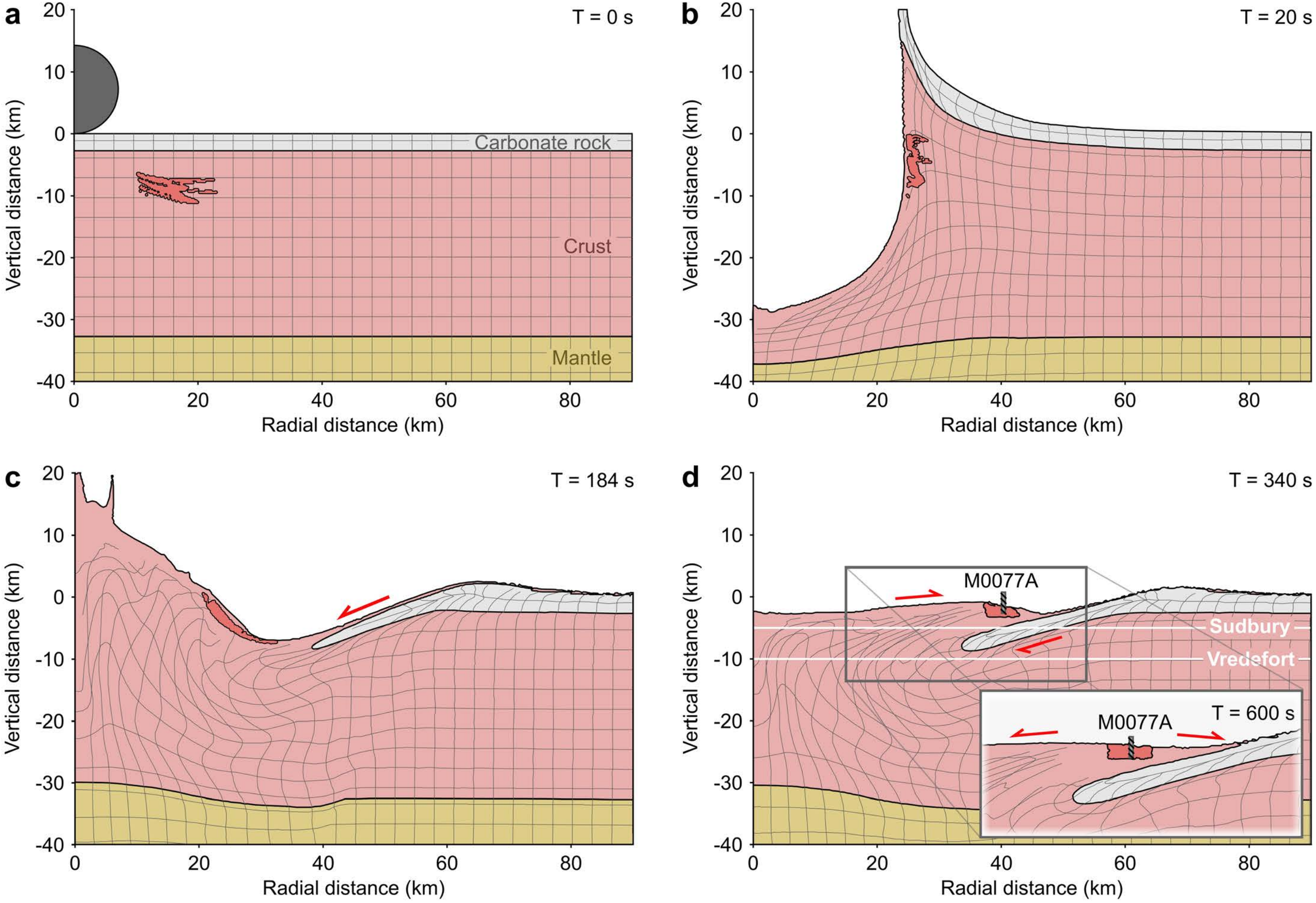
a
T = 0 s
Carbonate rock
Crust
Mantle
Vertical distance (km)
Radial distance (km)
b
T = 20 s
c
T = 184 s
d
T = 340 s
M0077A
Sudbury
Vredefort
T = 600 s

Cataclasite
Ultra-cataclasite
Shear faults
Crenulated foliations
Ductile band structures
mbsf
5 10 15 20
5
5 10 15
5 10 15 20 25 30
5 10 15 20 25 30
n = 166
n = 92
n = 602
n = 124
n = 121
750
800
850
900
950
1,000
1,050
1,100
1,150
1,200
1,250
1,300
Target rock
Fault breccia
Impact melt rock
Imbricate thrust zone

a

1 cm

b

C

1

kf

kf

kf

1 cm

c

2 cm

d

1 cm

e

500 µm

f

500 µm

g

2 cm

h

2 cm

i

2 cm

k

2 cm

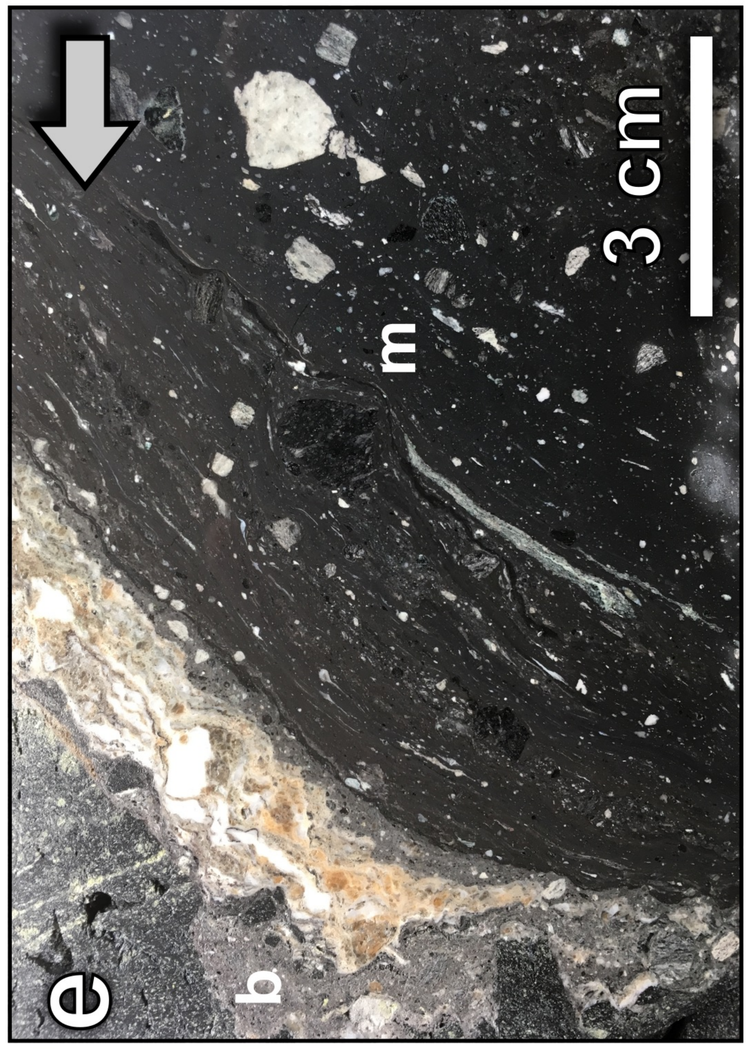

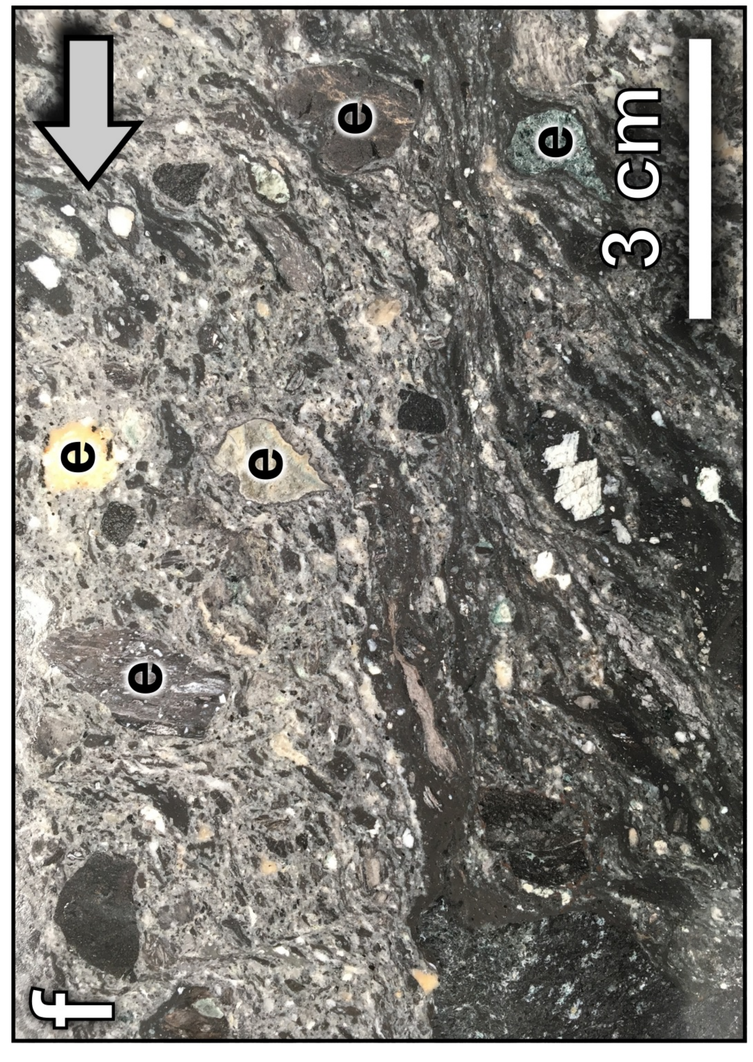

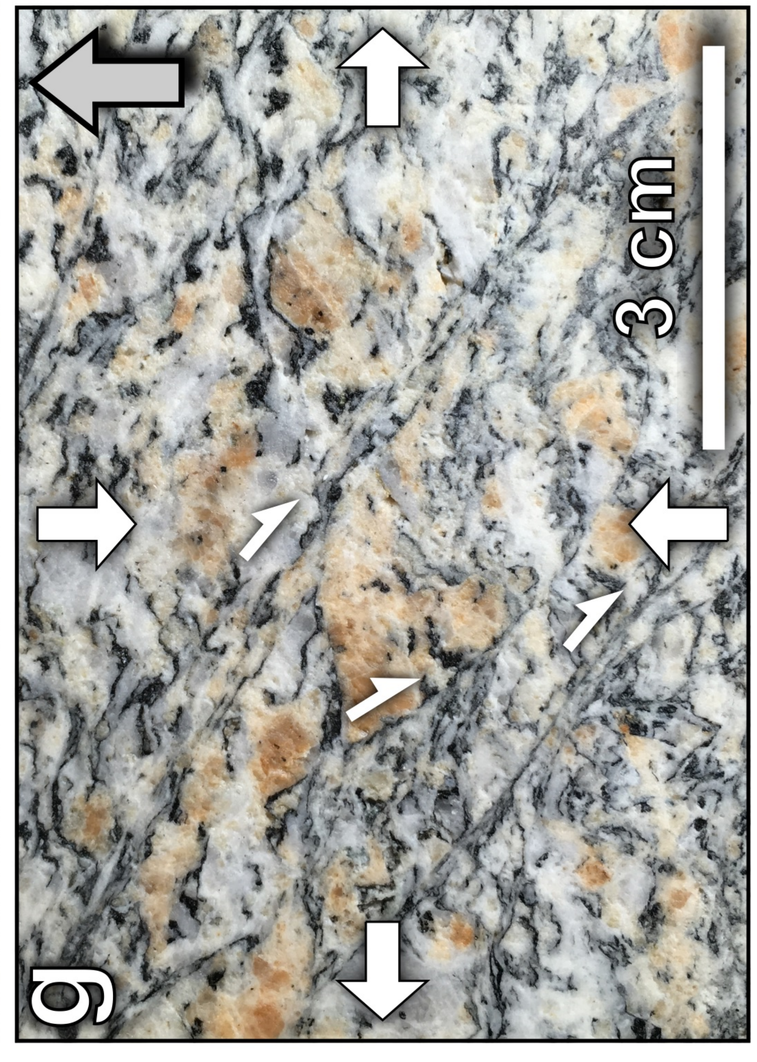

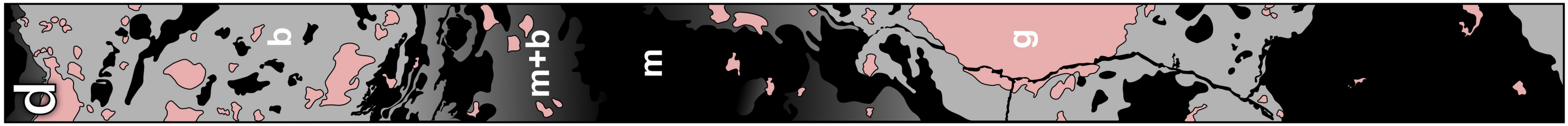

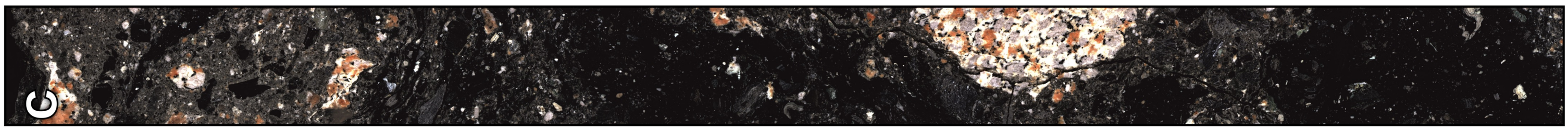

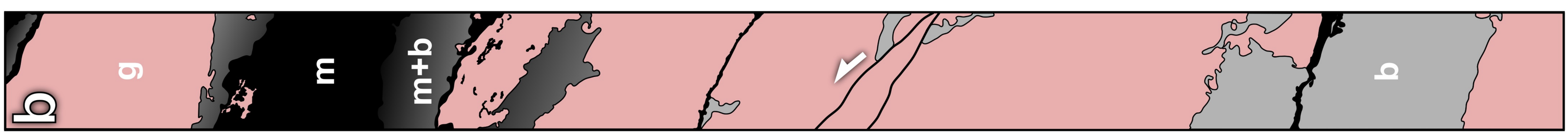

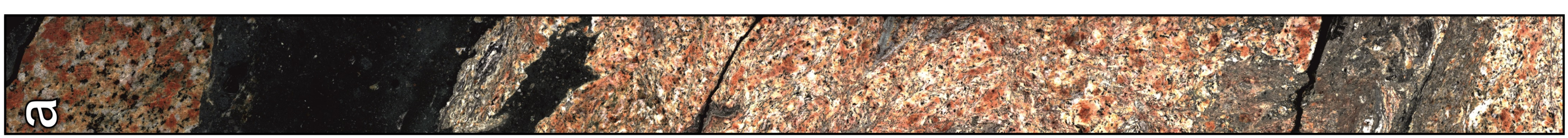

10 cm